# Volumetric imaging through a doubly-curved surface using a 2D phased array

Jessica G. McKee[1,a)], Rhodri L. T. Bevan[1], Paul D. Wilcox[1] and Robert E. Malkin[1]

[1] Department of Mechanical Engineering, University of Bristol, Bristol, BS8 1TR, UK

[a)] *Corresponding author: jessica.mckee@bristol.ac.uk*

**Abstract.** Ultrasonic phased arrays have become widely used in recent years in non-destructive testing (NDT). However, most NDT arrays are 1-dimensional (1D), which generate 2-dimensional (2D) images from a single position and lack the ability to focus accurately through surfaces that are curved in multiple directions. In this paper, a 2D phased array is used to experimentally image artificial defects (represented by bottom-drilled holes and electrical discharge machined notches) within a test specimen with a doubly-curved surface profile in an immersion configuration. The array is mechanically scanned above the entire surface of the specimen and the 3-dimensional (3D), or volumetric, images generated at each position are combined to produce a single image of the specimen's entire surface. The surface profile is then extracted and discretised for interior volumetric imaging. The results show that the root mean square (RMS) error between the ultrasonically extracted surface and the true surface is 0.04 mm and 95% of absolute errors are less than 0.07 mm. Finally, the positions of visible defects are measured, using (i) the depth above the back wall and (ii) the lateral distance from a notch on the specimen's surface, and compared to their true values. The study shows that the standard deviation of depth and lateral position measurements is 0.68 mm and 0.89 mm respectively. Defects that are located beneath regions of sufficiently steep surface curvature were unable to be imaged.

Keywords: Ultrasound, 2D phased array, volumetric imaging, TFM, FMC

## 1. Introduction

Ultrasonic waves have been utilised in many fields within the past century, such as structural health monitoring (SHM) [1,2] and non-destructive testing (NDT) [3–5]. Developments in NDT over the last few decades have made it possible to obtain accurate internal images of solid structures within the engineering design process, after part manufacture is completed and during service. Ultrasonic imaging involves transmitting a high-frequency pulse (generally in the 1 – 20 MHz range) into a component and processing the reflected signals to generate an image. Detecting and accurately characterising defects within solid structures is an essential part of many procedures to determine structural integrity and remaining component-life.

The use of traditional single-element probes in NDT inspections has many limitations, including the inability to vary focal depth, a restricted number of fixed directions available from which to detect defects, and the consequent potential for missing defects that are in unexpected positions or orientations. Phased arrays can be implemented to overcome some of these problems. Ultrasonic phased arrays are composed of many single-element transducers, and therefore have the benefits of electronic beam steering, focusing and scanning, which are made possible by applying delay laws to individually addressable elements [6]. As a direct result of these properties, phased arrays can be applied to a wider range of imaging scenarios and have the ability to speed up ultrasonic inspections dramatically, along with improving defect image resolution [7]. However, NDT inspections using phased arrays are currently limited to mainly 1-dimensional (1D) arrays with linear elements, and hence only 2-

dimensional (2D) slices of a component can be imaged from a single array position. A substantial limitation of using 1D arrays is that the steering is confined to a single plane and therefore they are unable to accurately focus through surfaces that are curved in multiple directions. There is also the possibility of missing scattering effects in the unreconstructed dimension, which means that there is a chance of missing defects that are in unexpected positions or orientations. By creating a 2D array with elements distributed across a 2D aperture it is possible to better characterise defects within components [8]. Similar to how 1D arrays allow beam steering within a 2D plane, 2D arrays enable beam manipulation throughout a 3-dimensional (3D) volume without requiring movement of the array. This ability significantly increases coverage of the imaging region, as long as the array and surface orientations are favourable, and it allows a more detailed inspection through volumetric beam steering and focusing [9].

Distinguishing between defect types is crucial for thorough and accurate inspections, as the severity of defects depends on their size, orientation and shape; for instance, it is well known that planar discontinuities (e.g. cracks) are usually more dangerous than volumetric defects (e.g. voids) due to their sharp edges that have the potential to grow and cause breaks. Therefore, obtaining 3D images of defects is desirable for precise defect characterisation. Volumetric inspections using a 1D array have previously been achieved by translating the array perpendicular to the 2D imaging plane and combining the resulting images together to reconstruct a 'pseudo-3D' volume from a series of 2D slices [10,11]. However, scattering effects in the unreconstructed dimension of the individual images are still not captured in this configuration.

A current area of interest in industry is the inspection of defects within regions where the surface geometry of a component curves in multiple directions, also known as doubly-curved surfaces, such as those found in pipework branches or nozzles. Current inspection procedures through these surfaces involve using either (i) a single-element transducer that probes the region from a range of locations, or (ii) radiographic methods. The use of a single-element transducer means that a highly-skilled operator needs to interpret the data and it is extremely challenging to build up a volumetric image of the region; while radiography is not very effective for detecting and sizing planar defects without prior knowledge of their likely location and orientation [12]. Due to the double curvature, 1D arrays are not ideal for inspecting through surfaces of this nature. Hence, the ability of 2D arrays to focus through doubly-curved surfaces presents a huge opportunity for improving the detection of defects within complex-shaped components.

For non-contact inspections, it is important to correctly account for the surface geometry in order to maintain a high image quality [13]. There are currently three main approaches to tackle ultrasonic inspections of this nature. The first of these involves using a liquid, such as water, to couple a rigid array to the surface of the component under inspection. The liquid acts as an acoustic couplant between the array and the component. The surface profile can be extracted from the ultrasonic data using an imaging algorithm [14,15], so previous knowledge of the surface is not required. In a previous study [16], a 2D array was used to generate 3D images in immersion; however, in this case the test specimen had a planar surface and determining the surface position from the data is straightforward. Another approach involves fitting the array with a wedge that compliments the surface geometry [17], however, each wedge is only suited to a single, known surface profile and so multiple wedges need to be constructed for the inspection of a complex component. A lesser-used hybrid method of these two approaches has also been considered, which involves a membrane-coupled phased array device [18]. The final

approach involves the use of a flexible contact array, in which the elements are capable of moving in the vertical direction as the array is translated over the surface [19,20].

In this paper, experimental defect imaging through a doubly-curved surface using a 2D phased array in an immersion setup is investigated. The data-capture format termed Full Matrix Capture (FMC) is utilised, along with the post-processing imaging algorithm termed the Total Focusing Method (TFM), both of which are explained in [21]. The array is mechanically scanned over the entire surface of a test specimen, where FMC datasets are captured at discrete overlapping array positions. A combining method ('stitching') is then implemented to fuse the 3D TFM images obtained from each position into a single, larger 3D TFM image. A 3D surface extraction method is also presented.

# 2. Experimental procedure

## 2.1 Array description

A 2D sparse array with elements arranged in a Poisson disk formation has been demonstrated to outperform a matrix array with the same number of elements, as the non-periodic element layout prevents the formation of grating effects while still maintaining a high level of imaging resolution [8]. For this reason, a 128-element 2D sparse array with 3 MHz centre frequency is used for this work. A description of the array is given in Table 1.

Table 1. 2D sparse array parameters.

| Array Parameter | Value |
|---|---|
| Element count | 128 |
| Element shape | Circular |
| Element diameter | 1.7 mm |
| Element pitch | ≥ 1.9 mm |
| Element spacing | ≥ 0.2 mm |
| Array aperture diameter | 30 mm |
| Centre frequency | 3 MHz |
| –6 dB bandwidth | ≥ 1.5 MHz |

## 2.2 Test specimen

To represent a doubly-curved surface geometry, an aluminium test specimen with a double-curved axisymmetric surface was manufactured, as shown in the side profile in Fig. 1(a). The surface was created with a Gaussian profile given by:

$$h = h_0 \exp(-\frac{r^2}{2\sigma^2}) \quad (1)$$

where $r$ is the radial distance from the peak, $h_0$ is the height of the peak and $\sigma$ is the standard deviation parameter of the Gaussian function. For this specimen, $h_0$ was 15 mm and $\sigma$ was 20 mm, so therefore the steepest angle of inclination on the surface was approximately 24° relative to the horizontal. The longitudinal velocity of sound in the specimen, $v_2$, was measured to be 6360 m/s, and hence the wavelength of sound at the centre frequency of the array, $\lambda_{Al}$, was 2.1 mm. 21 bottom-drilled holes (BDHs) were drilled into one side of the base of the specimen, with the tip of each hole on each radial arm from the peak at a different depth below the surface; the other side of the specimen contained four square electrical discharge machined (EDM) notches at different depths. The BDHs were drilled using a standard 120° inclusive drill bit of 3 mm diameter ($1.4\lambda_{Al}$) and the EDM notches were machined with a wire of 0.5 mm width ($0.2\lambda_{Al}$). A bottom-view of the specimen is shown in Fig. 1(b) with each defect labelled. The depth of each radial arm below the surface increased from 5 mm (corresponding to the arm

containing BDHs A-E) to 25 mm (corresponding to the arm containing BDHs R-U) in 5 mm increments. A 3 mm surface notch was drilled into the top surface of the specimen to act as a reference point for surface orientation and defect positioning.

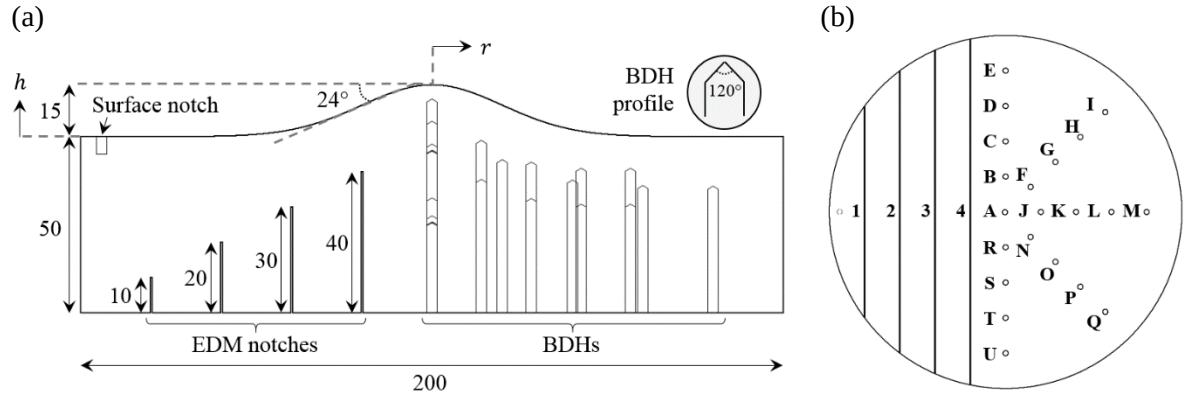


**Fig. 1.** Illustration of the designed specimen with machined defects. (a) shows the side profile and (b) shows the base view with the defects labelled. Units in mm.

The surface was independently measured using a laser scanner and the root mean square (RMS) error between the measured surface and that defined by Eq. (1) was found to be 0.06 mm and therefore in good agreement. For this reason, the ultrasonically extracted surface will be compared directly to the surface defined by Eq. (1).

## 2.3 Scanning procedure

A scanning tank with three translational degrees of freedom was used in order to perform a 2D scan over the entire surface of the specimen. Before scanning, the velocity of sound in water, $v_1$, was measured to be 1470 m/s which corresponded to a wavelength, $\lambda_W$, of 0.49 mm. To initialise the scan, the specimen was submerged in water and the array was mounted and aligned parallel to the back wall of the specimen using a B-scan image obtained over the flat region of the surface. The array was then set to a standoff distance of 13 mm above the peak of the specimen, before being moved to the scan start location. A schematic diagram of the experimental setup is shown in Fig. 2. The total scanned area was 240 mm x 240 mm using a total of 225 individual array positions at a pitch of 15 mm in $x$ and $y$, resulting in an array aperture overlap of 50% between adjacent positions. The total time to complete the scan was approximately 2 hours. Time-data was captured at each position with 10 averages, then filtered and Hilbert transformed using a Gaussian window function centred at the array centre frequency with a -40 dB half bandwidth of 90% of the array centre frequency.

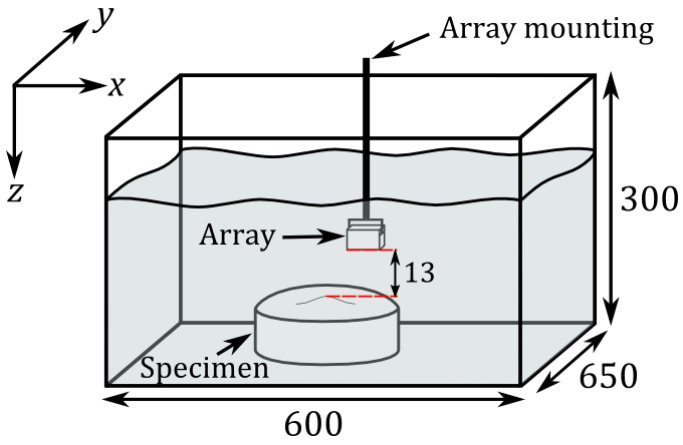


**Fig. 2.** Illustration showing the scanning tank apparatus used to scan the surface of the specimen across the 2D $(x - y)$ plane. The standoff between the peak of the specimen and the array was 13 mm. Units in mm.

# 3. Image processing methods

Data captured using FMC format contains the time-domain signals (A-scans) of all transmit-receive element pair combinations in the array and enables offline post-processing of the data [21]. TFM imaging is a post-processing algorithm that uses time-domain signals that are stored in FMC format, and generates a fully-focused image by creating an effective focus of the ultrasonic beam at each location in a defined imaging grid. It has been shown that TFM imaging produces high resolution images when compared to other imaging techniques [21] and is hence used throughout this work. As different methods have been used to generate volumetric images in the past, it is worth clarifying that the method described and implemented here involves capturing a single FMC dataset from each array position and stitching all resulting 3D TFM images together. A similar stitching method was used in [14] in the context of 2D imaging using a 1D array, whereby multiple small TFM images with overlapping regions were stitched to produce an image that was larger in size than the individual images.

TFM imaging is able to synthetically focus ultrasonic signals at every location in an imaging grid by sampling the A-scan corresponding to each transmit-receive element pair at a time that corresponds to the time-of-flight (TOF) of the ray path between the elements and image point. For imaging in a single medium, the TOF is easily obtained through basic trigonometry. An illustration of a ray in single-medium 3D imaging is shown in Fig. 3(a), where the pulse travels between points $\mathbf{E}_T$, $\mathbf{P_1}$ and $\mathbf{E}_R$, which are the position vectors of the transmitting element, image point and receiving element respectively. This journey consists of two 'legs', where each leg is a section of the ray path between two points and only $v_1$ is required to calculate the TOF. The dotted lines in Fig. 3(a) correspond to the surface of the specimen, which is unknown at this stage. The challenge of finding the TOF is harder in the case of dual media with different acoustic velocities, as in the case of immersion imaging. The solution is obtained by using Fermat's principle of least time [22] to determine the two surface-crossing points that yield the global minimum total TOF between the element pair and each image point. An illustration of the path that results in the minimum TOF between $\mathbf{E}_T$, $\mathbf{P_2}$ and $\mathbf{E}_R$ is shown in Fig. 3(b) where $v_2$ now also needs to be taken into consideration. The path connects the transmitting element $\mathbf{E}_T$, to the first surface-crossing location $\mathbf{A}_T$, to image point $\mathbf{P_2}$, to the second surface-crossing location $\mathbf{A}_R$ and finally to the receiving element $\mathbf{E}_R$.

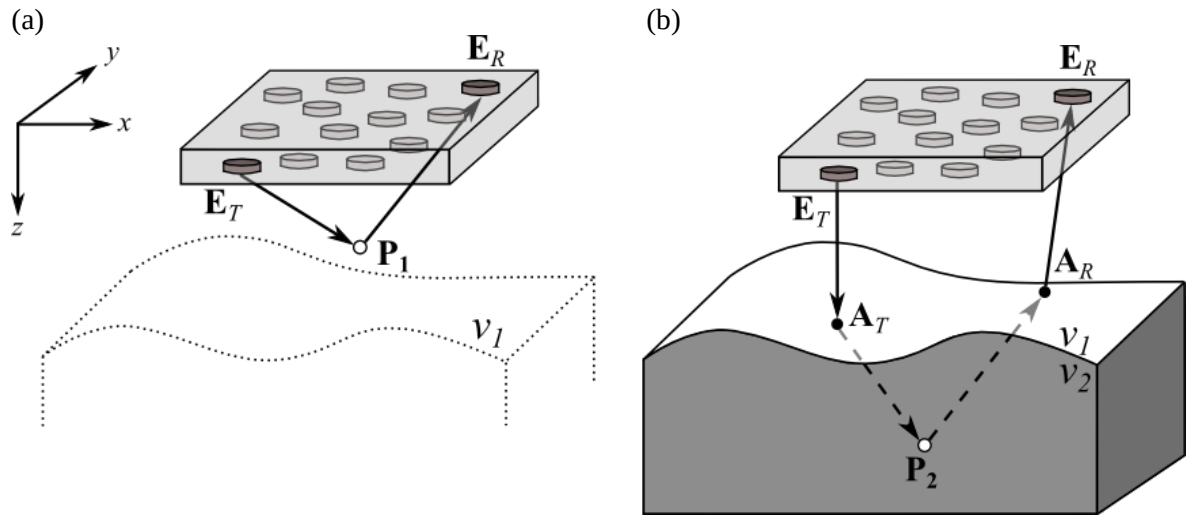


**Fig. 3.** 3D imaging illustration of a ray path in (a) single medium and (b) immersion that yields the global minimum TOF between $\boldsymbol{E_T}$, $\boldsymbol{P_1}$ or $\boldsymbol{P_2}$, and $\boldsymbol{E_R}$ using a 2D phased array. The outline of the unknown surface of the specimen is shown by the dotted lines in (a) and plays no part in the calculation of the ray path in this case. Solid arrows represent rays travelling in water, while dashed arrows represent rays travelling in the specimen.

3D TFM imaging through an arbitrary surface in an immersion setup is achieved using a two-stage process detailed below.

## 3.1 Stage I: Surface extraction

The first step to experimentally extract the surface profile of the specimen is to implement a single-medium TFM algorithm for each FMC dataset using only $v_1$, as shown in Fig. 3(a). The location of the surface is unknown at this point and therefore the imaging grid needs to be large enough to cover the potential surface region underneath each array position. The surface at each position was assumed to be at the location of the first reflection in the time-domain data. For an arbitrary image point $\mathbf{P_1}$, the image intensity, $I_{surf}(\mathbf{P_1})$, for each transmit-receive element pair is calculated using:

$$I_{surf}(\mathbf{P_1}) = \left|\sum a_{T,R}\, h_{T,R}\left(\frac{\|\mathbf{E}_T-\mathbf{P_1}\|+\|\mathbf{E}_R-\mathbf{P_1}\|}{v_1}\right)\right| \quad (2)$$

where the summation is over all transmit, $T$, and receive, $R$, element combinations. $a_{T,R}$ denotes an optional apodisation term [23] which is unused in this work, hence $a_{T,R} = 1$. $h_{T,R}(t)$ represents the complex Hilbert transform of the A-scan corresponding to transmitting from $T$ and receiving on $R$. Lanczos interpolation of $h_{T,R}(t)$, using a kernel size of 3, is utilised to sample from the discrete time domain signal and $\|\cdot\|$ denotes the Euclidean norm of a vector.

When stitching the image data from all array positions together, the maximum amplitude of overlapping image points (i.e. points that were imaged in more than one array position) is taken as the true amplitude. Up to this point, no reference is made to the component under inspection and the result is a stitched single-medium 3D TFM image of the entire surface of the specimen. Due to the complex nature of the specimen's surface and the orientation of the probe relative to the surface, there is a variation of reflected surface signal strength. This presents an issue as simply taking the points that are above a specified threshold amplitude to define the location of the specimen surface results in a discontinuous surface, therefore a more sophisticated, two-pass surface extraction process is required. This process is outlined below.

A discrete point in the imaging grid is defined as $\mathbf{P}_{ijk} = (x_i, y_j, z_k)$, where $x_i$ denotes equally spaced points in $x$, and similarly for $y_j$ and $z_k$. The image amplitude at this point is then obtained by $I_{ijk} = |I_{surf}(\mathbf{P}_{ijk})|$. The first step of the extraction process is to find the indices $(i, j, k) = (I, J, K)$ of the location of the maximum amplitude in the stitched TFM image using:

$$(I, J, K) = \underset{(i,j,k)}{\operatorname{argmax}}\ I_{ijk} \tag{3}$$

and therefore $\mathbf{P}_{IJK} = (x_I, y_J, z_K)$ is taken as the first point of the extraction process. Let $Z_{ij}^{(1)}$ denote the 3D surface points that are to be determined. The first surface point obtained in $Z_{ij}^{(1)}$ is the value of the $z$ coordinate at the position of the global maximum found above:

$$Z_{IJ}^{(1)} = z_K. \tag{4}$$

In the first pass, the primary and secondary directions are $x$ and $y$ respectively. The 2D $(x - z)$ plane through $y_J$ is examined first by working out from $(i, j) = (I, J)$ in the primary direction. The next surface point in the $x$ direction, i.e. $(i, j) = (I + 1, J)$, is found by fitting a spline, $S(z)$, to the image amplitudes, $I_{(I+1)Jk}$, at $k$-indices that satisfy

$$Z_{IJ}^{(1)} - \delta z \leq z_k \leq Z_{IJ}^{(1)} + \delta z, \tag{5}$$

where $\delta z$ is a predefined tolerance parameter, in this case set to approximately $1.2\lambda_W$. If the maximum of $S(z)$ exceeds a predefined threshold, then the $z$ coordinate of the next surface point is defined as:

$$Z_{(I+1)J}^{(1)} = \underset{z}{\operatorname{argmax}}\, S(z), \tag{6}$$

with the procedure shown in Fig. 4(a). If no value is found in the range of Eq. (5) that satisfies the amplitude threshold, the surface point at $Z_{(I+1)J}^{(1)}$ is defined as absent and the next position in the primary direction, $(i, j) = (I + 2, J)$, is considered instead. This is repeated until a valid point is found. At each absent point the value of $\delta z$ is slightly increased in case there is a small gap in the surface that can be bridged. When a valid surface point is found the process is then repeated from Equation (5) starting at that point. This is repeated until 10 consecutive absent points are encountered, corresponding to $6\lambda_W$, which is assumed to indicate that the edge of the measurable surface has been reached. Surface points in the negative $x$ direction from $\mathbf{P}_{IJK}$, i.e. $(i, j) = (I - 1, J)$, are then extracted until the other edge of the surface is reached. This extraction is shown in Fig. 4(b), where the primary direction is shown by the red arrow and the extracted points along the plane are shown by the blue dots.

The surface is then extracted in the secondary direction. This is achieved by starting with each of the previously extracted surface points in the primary direction and applying the same process in the secondary direction. This is shown by the dashed grey arrows in Fig. 4(b) and $Z_{ij}^{(1)}$ is now filled with the $x, y, z$ coordinates of the extracted surface. This concludes the first pass of the surface extraction process.

In the second pass, the entire extraction process is then repeated, only this time with $y$ as the primary and $x$ as the secondary direction, as illustrated in Fig. 4(c). This yields a second estimate of the surface profile, $Z_{ij}^{(2)}$.

The fully-extracted 3D surface, $Z_{ij}$, is then found by averaging the two extracted surfaces:

$$Z_{ij} = \frac{z_{ij}^{(1)} + z_{ij}^{(2)}}{2}. \quad (7)$$

The reasoning behind extracting the surface in two passes is to ensure reliable coverage of the surface, independent of the starting point. This would not necessarily be achieved in a single pass, as shown by the blank region at the top left of Fig. 4(c).

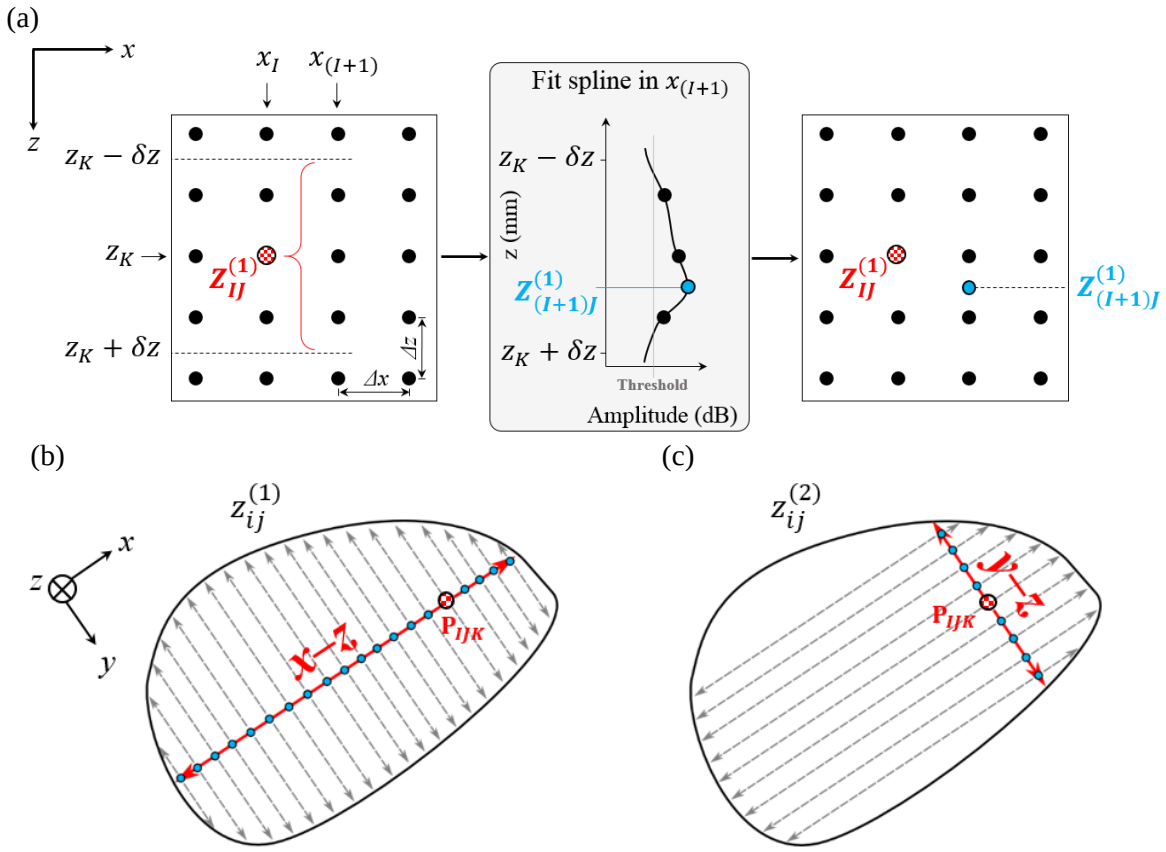


**Fig. 4.** Illustration of the surface extraction method on an arbitrary-shaped surface. (a) Shows the process of finding the location of an extracted surface at an adjacent $x$ position with a $z$ constraint of $\pm\delta z$ applied, where $\Delta x$ and $\Delta z$ represent the grid spacing in the $x$ and $z$ axes, while (b) and (c) show the top view of the extraction directions. In (b) and (c), the red checkered dot symbolizes the starting point of the extraction process, the blue dots symbolize extracted surface points along the red primary extraction direction and the dashed grey arrows show the secondary extraction direction.

The extracted surface, $Z_{ij}$, is used in the second imaging stage. It was also compared to the true surface generated using Eq. (1) to obtain the $z$ position error at each surface point.

## 3.2 Stage II: Interior imaging

To image the interior of the specimen, a second set of TOFs are calculated while considering the extracted surface points and velocity of sound in each medium, as shown in Fig. 3(b). For each array position, a subset of the extracted surface points is considered for TOF calculations for computational time and practicality reasons. Only points within a certain distance of the vertical line through the centre of the array (i.e. points within a cylinder relative to the array axis) are considered. Fermat's principle is applied to determine the surface crossing points and TOFs. The TOFs from the extracted surface points to an arbitrary image point, $\mathbf{P_2}$, are calculated and stored, as are the TOFs from each surface point to an array element, $\mathbf{E}_\beta$, where $\beta = T, R$. The surface point, $\mathbf{A}_\beta$, corresponding to the global minimum TOF between $\mathbf{E}_\beta$ and $\mathbf{P_2}$ is found, which represents the true ray path from that element in either transmission ($\beta = T$) or reception ($\beta = R$). By using this result, the intensity of the image, $I(\mathbf{P_2})$, at any image

point in the interior imaging grid is calculated by summing over all $T$ and $R$ combinations using:

$$I(\mathbf{P_2}) = \left| \sum a_{T,R}\, h_{T,R}\left( \frac{\|\mathbf{E}_T - \mathbf{A}_T\|}{v_1} + \frac{\|\mathbf{A}_T - \mathbf{P_2}\|}{v_2} + \frac{\|\mathbf{P_2} - \mathbf{A}_R\|}{v_2} + \frac{\|\mathbf{A}_R - \mathbf{E}_R\|}{v_1} \right) \right| \quad (8)$$

where Lanczos interpolation is used to query $h_{T,R}(t)$ at indiscrete times and $a_{T,R} = 1$.

All interior TFM images from each array position are then stitched together to create a 3D TFM image of the entire interior of the specimen. A summarized outline of the entire imaging process is described in the Appendix.

# 4. Experimental results

The stitched 3D surface TFM image is shown as an isosurface in Fig. 5(a). The isosurface is plotted at -10 dB relative to the maximum amplitude and coloured according to depth in the $z$ axis. The $z$ axis represents distance below the array, which was positioned at $z = 0$ mm. Fig. 5(b) shows the associated positional error in $z$, $\Lambda_z$, between the ultrasonically extracted surface and the true surface given in Eq. (1). The RMS error is 0.04 mm, the maximum absolute error is 0.3 mm and the surface notch location is evident at ($x$ =100, $y$ =195) mm in Fig. 5(b).

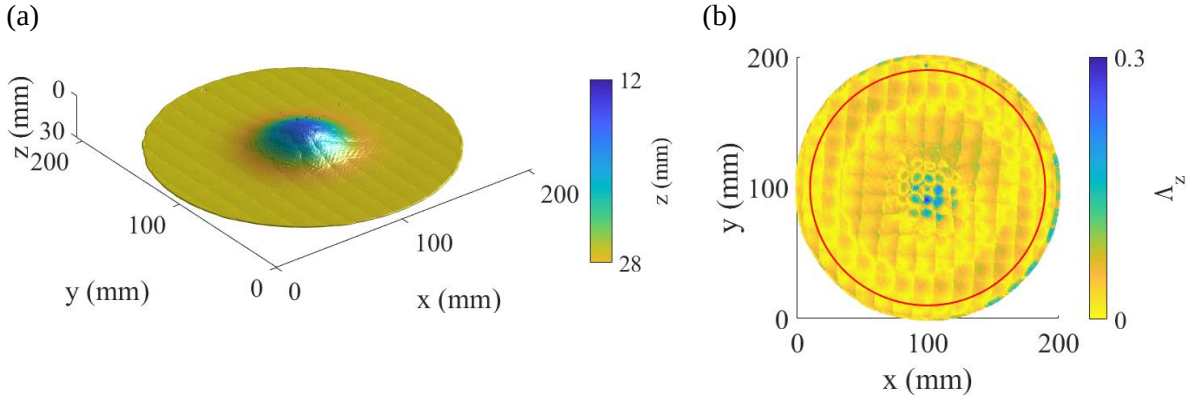


**Fig. 5.** (a) The ultrasonically extracted stitched 3D surface TFM image plotted as an isosurface at -10 dB. (b) Positional error in $z$, $\Lambda_z$, between the ultrasonically extracted surface and the true surface represented by Eq. (1). Only $\Lambda_z$ values within a 90 mm radius from the peak in (b), shown by the red circle, are considered when calculating the RMS and absolute errors to avoid the errors from the notch and edge skewing the results.

The stitched 3D interior TFM image of the specimen is shown as an isosurface in Fig. 6, plotted at -24 dB relative to, or approximately 6% of, the maximum amplitude in the back wall. By windowing the regions around the defects in Fig. 6, individual snapshots of the visible defects are obtained and a selection of them are shown in Fig. 7. EDM notches 1 and 4 are shown in Fig. 7(a) and (b), while BDHs O, P and Q are shown in Fig. 7(c), (d) and (e) respectively.

It was found that the defects located under the region of steep inclination are unable to be imaged at any reasonable amplitude level, as is evident by the gap in the isosurface plot of EDM notch 4 in Fig. 7(b). For this reason, BDHs B, F, J, N and R are excluded from the results. BDH C is also excluded as the signal-to-noise ratio (SNR) is too low for imaging. The central location of each BDH and EDM notch was found by taking the mean of the locations of points whose amplitudes were greater than or equal to 6 dB below the local maximum amplitude. Each defect is plotted at the central location using multiple isosurfaces at different amplitude levels relative to the maximum amplitude in the back wall.

The positioning of defects is investigated within the specimen and is found using two methods. The first involves measuring the depth of each defect above the back wall, and the second involves measuring the lateral distance of each defect from the surface notch. These distances are then compared to the true values from the specimen design file from Fig. 1, with the results shown in Fig. 8(a) and (b) respectively. The standard deviation of depth and lateral distance from the surface notch measurements is 0.68 mm and 0.89 mm respectively.

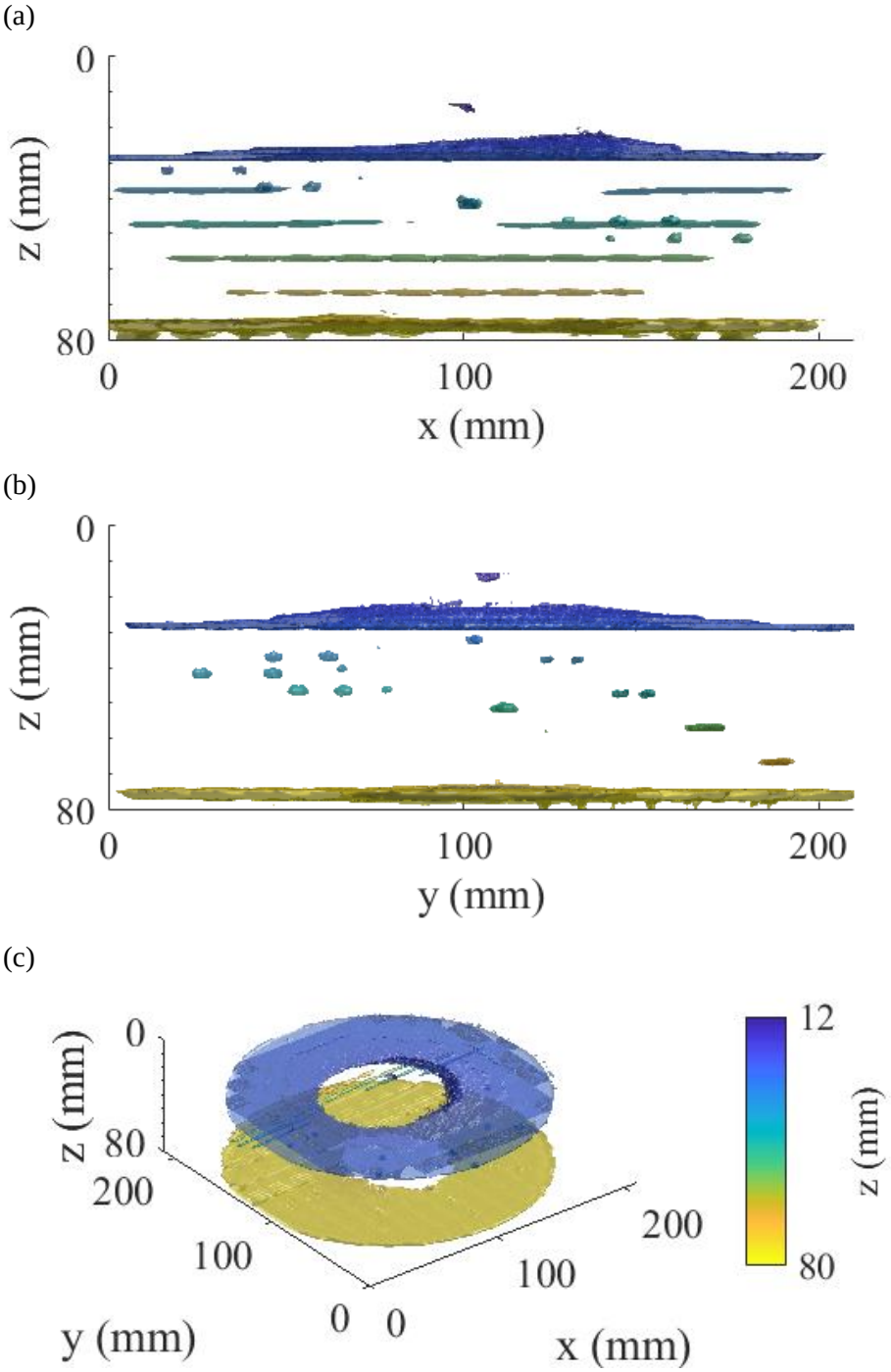


**Fig. 6.** Stitched 3D interior TFM image of the specimen plotted as an isosurface at -24 dB relative to the maximum amplitude in the back wall and coloured according to distance in *z*. (a) and (b) show elevations, while (c) shows a 3D view.

(a) (c)

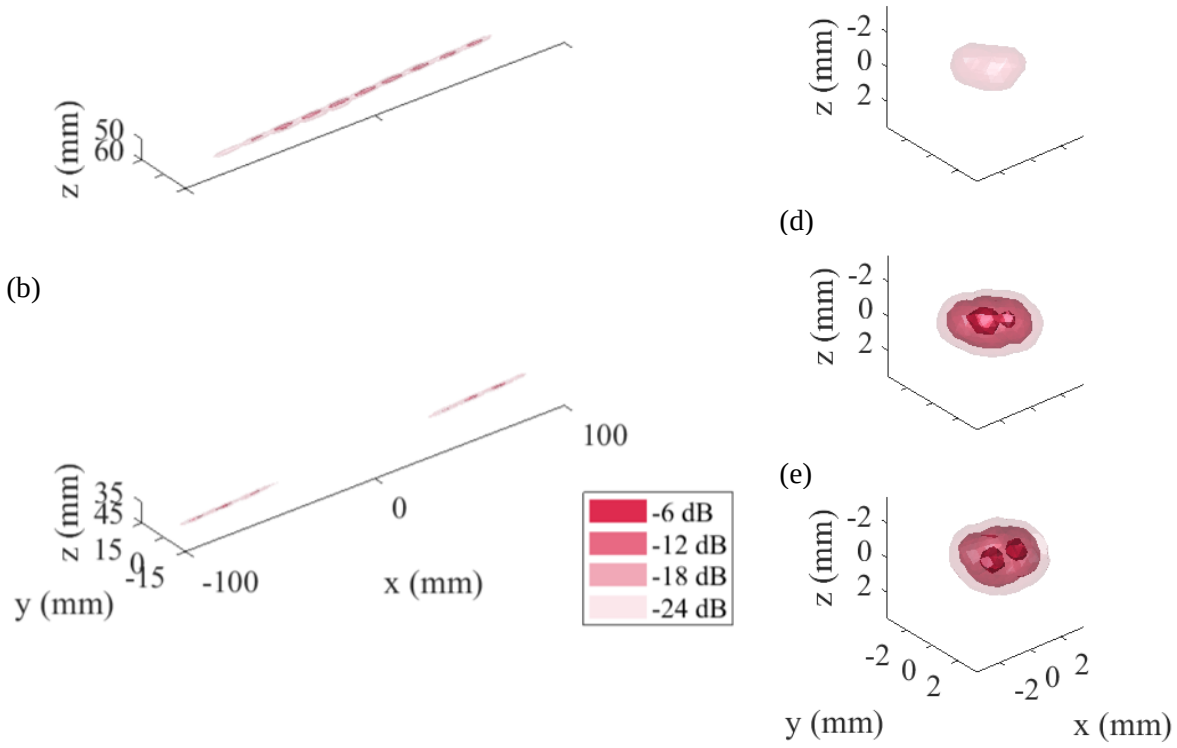


**Fig. 7.** 3D TFM images of EDM notches (a) 1, (b) 4, and BDHs (c) O, (d) P and (e) Q, plotted as multiple isosurfaces at different dB levels relative to the maximum amplitude in the back wall. Defects shown at nominal positions.

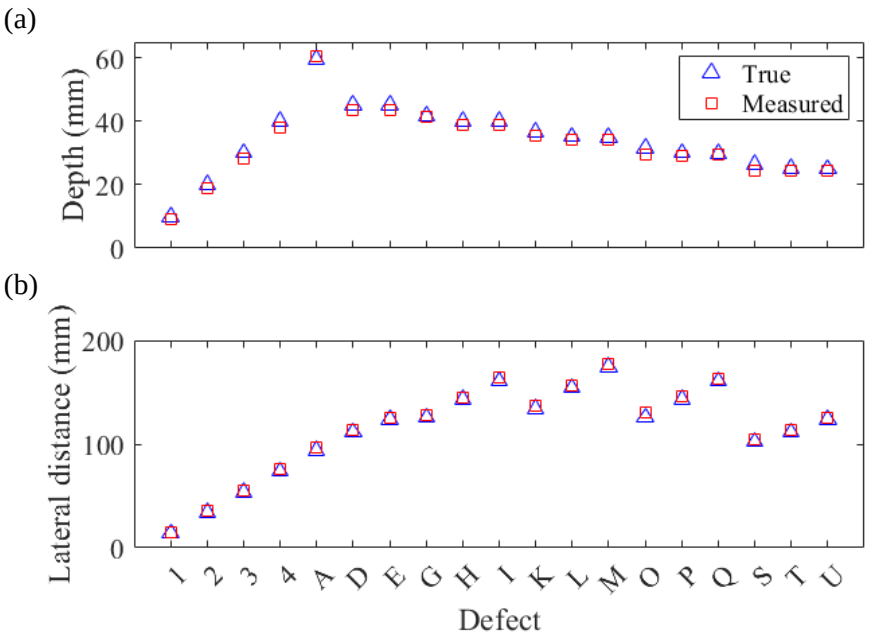


**Fig. 8.** Comparison of measured and true defect positions. (a) Shows the comparison of the depth of the defects above the back wall of the specimen and (b) shows the comparison of lateral defect distance from the surface notch.

# 5. Discussion

The surface extraction algorithm produced a surface that was in close agreement with the designed surface, as shown in Fig. 5(b), as 95% of absolute errors between the extracted and true surfaces are less than 0.07 mm. The gridded appearance visible in the stitched surface TFM in Fig. 5(a) is due to the stitching algorithm, whereby the maximum amplitudes of image points in the overlapped regions are taken as the true amplitudes. The $x$ and $y$ lengths of the imaging region for each array position was twice the diameter of the array, and so the presence of imaging artefacts in overlapped regions results in a slightly distorted image. However, applying an angle limit during the imaging process would reduce or eliminate artefact appearance.

From observing the result in Fig. 6, it is evident that some defects are visible, while others are not. The peak of the surface is not visible in Fig. 6 as the isosurface was plotted at a single contour level and due to the surface inclination angle and the orientation of the array, the amplitude of the inclined surface regions are much lower than that of the flat regions. Defects not located directly under the steep inclination region are visible and in the intended locations, as evidenced by Fig. 8. Fig. 9 shows the inclination along the surface of the specimen and includes the positions of the BDHs and EDM notches. Defects under the region of the surface with an approximate inclination larger than the longitudinal critical angle for a wave travelling from water to aluminium, $\theta_c$ = 13.4°, proved impossible to image using this setup orientation. EDM notch 4, shown in Fig. 7(b), illustrates this as there is a gap in the isosurface as part of the notch is underneath the region of highest inclination. The BDHs that were unable to be imaged include BDHs B, F, J, N and R, along with BDH C due to its low SNR and are coloured white in the figure. The reason for low SNR on BDH C is due to it lying on the radial arm that was drilled at the smallest depth below the surface. The reason for the other defects not being imaged is due to several factors. Firstly, consider the surface to be an inclined plane with a steepest angle of 24° and the array positioned directly above the steepest surface location. In the region of the sample directly under the array, the majority of the incident energy is reflected due to the surface angle being larger than $\theta_c$. To the side of the array further up the plane, there is a region where rays from the array are incident on the surface below $\theta_c$. However, the directivity amplitude of the elements in the array means that there is low transmission and reception sensitivity in these directions as they are at relatively large angles relative to the array normal. Fig. 10 shows the directivity, $D(\phi)$, of a 1.7 mm diameter circular element radiating into water at 3 MHz, calculated using:

$$D(\phi) = \frac{2J_1(kb\sin\phi)}{kb\sin\phi} \tag{9}$$

from [24] where $J_1$ is the 1$^{st}$ order Bessel function, $k$ is the wavenumber, $b$ is the element radius and $\phi$ is an angle relative to the element normal. $D(\phi)$ represents the directivity on transmission and reception, so to obtain the total directivity for a transmit-receive element pair their individual directivities at the respective angles are calculated and multiplied together. The array elements' highest sensitivity is at 0°, which corresponds to the direction directly beneath the element. For a planar surface parallel to the base of the array, the directivity of the elements is therefore the highest, as shown in the $\pm\theta_c$ range by the solid blue line in Fig. 10. However, for a surface inclination of 24°, as shown by the dashed red region of the graph, the directivity within the $24° \pm \theta_c$ range is much lower. For this surface inclination the elements have reduced sensitivity to any signals entering or leaving the specimen. The ratio of the average directivity in the parallel surface case when compared to the inclined surface case is approximately 20:1. By examining BDHs O, P and Q in Fig. 7(c), (d) and (e) respectively, this effect is evident as the average amplitude in BDH O is approximately 10 dB lower than that in BDHs P and Q, illustrating that defects located under the inclined region have lower amplitudes when

compared to defects located under a planar surface parallel to the array. From Fig. 8(a) and (b) it can be seen that the true and measured values closely agree for visible defects.

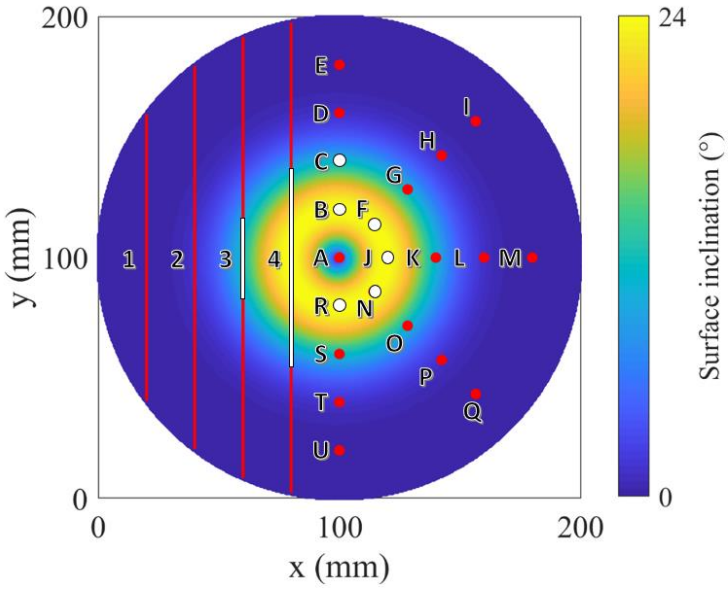


**Fig. 9.** Surface inclination with the locations of the EDM notches and BDHs marked. White circles represent defects that were unable to imaged and white lines represent portions of EDM notches that were unable to be imaged.

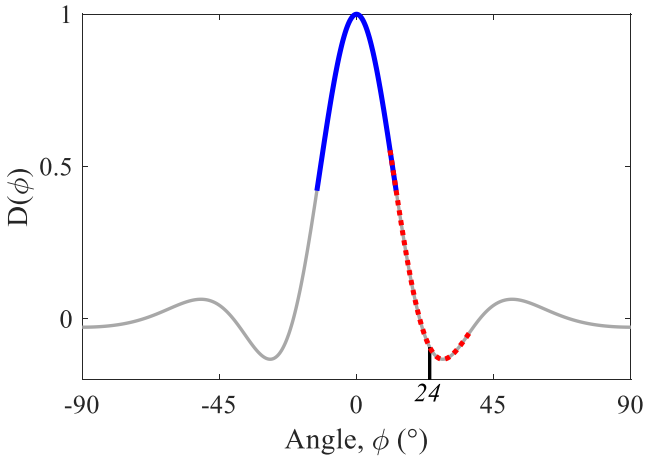


**Fig. 10.** The directivity of a 1.7 mm diameter circular element radiating into water at 3 MHz as a function of angle relative to the element normal direction. The solid blue region is the range $\pm\theta_C$ and the dashed red region is the range $24°\pm\theta_C$.

The surface spatial resolution was 0.3 mm, which was just below $\lambda_W$, and the interior TFM spatial resolution was set to $\lambda_{Al}/4$, or half of the diffraction limit of the longitudinal wavelength. The runtime on a desktop computer for the entire imaging process was 40 hours (Intel Core i7-6700 3.4 GHz quad-core processor; 16 GB RAM, Quadro K620 GPU).

## 6. Conclusion

With the advances in ultrasonic imaging over the past few years, the use of 2D phased arrays for volumetric imaging has the potential to open the door to many new imaging applications. The use of FMC and TFM in this work has demonstrated the ability of 2D arrays to volumetrically image defects through an unknown doubly-curved surface, provided the surface

and array orientation is favourable. Defects that were able to be imaged were well focused, but defects positioned in locations beneath a relatively steep surface inclination were unable to be imaged for multiple reasons, such as unfavourable orientation of the array and surface, along with element directivity. The extracted surface profile was in very good agreement with the true surface as the RMS error between them was 0.40 mm and 95% of absolute error values were less than 0.07 mm. Although the surface extraction method was successful when extracting this surface, it does need further investigation as it may not work as well on more complex surfaces, such as those with discontinuities or very steep interfaces. A possible solution could involve extracting surface points using the four nearest neighbours around each point, instead of extracting along 2D planes as was demonstrated here. When considering the positioning of defects, it was found that the standard deviation of depth and lateral distance from the surface notch measurements is 0.68 mm and 0.89 mm respectively. This illustrates that the measured positions of the defects which could be imaged agreed with the true locations. As the average amplitudes of identical BDHs decreases with increasing surface inclination, erroneous imaging results may be obtained. The severity of a defect is not taken simply by its amplitude, so some defects may be missed by thresholding the images at an amplitude level.

Future work will involve work on the sizing flat-bottomed holes and round-bottomed holes through a similar surface profile to simulate the sizing of cracks and voids. A more advanced stitching method could also be investigated to improve the calculation of amplitudes in overlapped regions, along with investigating methods of compensating for amplitude scaling through the use of sensitivity maps. Another investigative avenue could focus on the optimisation of the imaging algorithm to potentially speed up the computational process.

# Acknowledgement

This work was supported by Frazer-Nash Consultancy.

# References

[1] Lowe MJS, Alleyne DN, Cawley P. Defect detection in pipes using guided waves. Ultrasonics 1998;36:147–54. https://doi.org/10.1016/S0041-624X(97)00038-3.

[2] Croxford AJ, Wilcox PD, Drinkwater BW, Konstantindis G. Strategies for guided-wave structural health monitoring. Proc R Soc A 2007;463:2961–81. https://doi.org/10.1098/rspa.2007.0048.

[3] Pudovikov S, Bulavinov A, Pinchuk R. Innovative ultrasonic testing (UT) of nuclear components by sampling phased array with 3D visualization of inspection results. 8th Int. Conf. NDE Relat. to Struct. Integr. Nucl. Press. Components, 2010.

[4] Amenabar I, Mendikute A, López-Arraiza A, Lizaranzu M, Aurrekoetxea J. Comparison and analysis of non-destructive testing techniques suitable for delamination inspection in wind turbine blades. Compos Part B Eng 2011;42:1298–305. https://doi.org/10.1016/j.compositesb.2011.01.025.

[5] Clark R. Rail flaw detection: overview and needs for future developments. NDT E Int 2004;37:111–8. https://doi.org/10.1016/j.ndteint.2003.06.002.

[6] Wilcox PD, Holmes C, Drinkwater BW. Enhanced defect detection and characterisation by signal processing of ultrasonic array data. Proc. 9th ECNDT, 2006.

[7] Drinkwater BW, Wilcox PD. Ultrasonic arrays for non-destructive evaluation: A review. NDT E Int 2006;39:525–41. https://doi.org/10.1016/j.ndteint.2006.03.006.

[8] Velichko A, Wilcox PD, Thompson DO, Chimenti DE. Defect characterization using two-dimensional arrays. Rev. Prog. Quant. Nondestruct. Eval., 2011, p. 835–42. https://doi.org/10.1063/1.3591934.

[9] Wilcox PD. Ultrasonic arrays in NDE: Beyond the B-scan. Rev Prog Quant Nondestruct Eval 2013;1511:33–50. https://doi.org/10.1063/1.4789029.

[10] Sun C, Gang T, Peng Y. Ultrasonic phased array three-dimensional imaging using TFM-based slice. 19th World Conf. Non-Destructive Test., 2016.

[11] Kerr W, Rowe P, Pierce SG. Accurate 3D reconstruction of bony surfaces using ultrasonic synthetic aperture techniques for robotic knee arthroplasty. Comput Med Imaging Graph 2017;58:23–32. https://doi.org/10.1016/j.compmedimag.2017.03.002.

[12] Ditchburn RJ, Burke SK, Scala CM. NDT of welds: state of the art. NDT E Int 1996;29:111–7. https://doi.org/10.1016/0963-8695(96)00010-2.

[13] Hunter AJ, Drinkwater BW, Wilcox PD. Autofocusing ultrasonic imagery for non-destructive testing and evaluation of specimens with complicated geometries. NDT E Int 2010;43:78–85. https://doi.org/10.1016/j.ndteint.2009.09.001.

[14] Malkin RE, Franklin AC, Bevan RLT, Kikura H, Drinkwater BW. Surface reconstruction accuracy using ultrasonic arrays: Application to non-destructive testing. NDT E Int 2018;96:26–34. https://doi.org/10.1016/j.ndteint.2018.03.004.

[15] Le Jeune L, Robert S, Dumas P, Membre A, Prada C. Adaptive ultrasonic imaging with the total focusing method for inspection of complex components immersed in water. Rev. Prog. Quant. Nondestruct. Eval., Boise, Idaho: 2015, p. 1037–46. https://doi.org/10.1063/1.4914712.

[16] Tweedie A, O'Leary RL, Harvey G, Gachagan A, Holmes C, Wilcox PD, et al. Total focussing method for volumetric imaging in immersion non destructive evaluation. 2007 IEEE Ultrason. Symp. Proc., IEEE; 2007, p. 1017–20. https://doi.org/10.1109/ULTSYM.2007.259.

[17] Drinkwater BW, Bowler AI. Ultrasonic array inspection of the Clifton Suspension Bridge chain-links. Insight - Non-Destructive Test Cond Monit 2009;51:491–8. https://doi.org/10.1784/insi.2009.51.9.491.

[18] Russell J, Long R, Cawley P. Development of a twin crystal membrane coupled conformable phased array for the inspection of austenitic welds. Rev Prog Quant Nondestruct Eval 2011;30:811–8. https://doi.org/10.1063/1.3591931.

[19] Roy O, Mahaut S, Casula O. Control of the ultrasonic beam transmitted through an irregular profile using a smart flexible transducer: modelling and application. Ultrasonics 2002;40:243–6. https://doi.org/10.1016/S0041-624X(02)00145-2.

[20] Casula O, Poidevin C, Cattiaux G, Fleury G. A flexible phased array transducer for contact examination of components with complex geometry. Proc. 16th World Conf. NDT, 2004.

[21] Holmes C, Drinkwater BW, Wilcox PD. Post-processing of the full matrix of ultrasonic transmit–receive array data for non-destructive evaluation. NDT E Int 2005;38:701–11. https://doi.org/10.1016/j.ndteint.2005.04.002.

[22] Schuster A. An introduction to the theory of optics. 1909.

[23] Bevan RLT, Zhang J, Budyn N, Croxford AJ, Wilcox PD. Experimental quantification of noise in linear ultrasonic imaging. IEEE Trans Ultrason Ferroelectr Freq Control 2019;66:79–90. https://doi.org/10.1109/TUFFC.2018.2874720.

[24] Kinsler LE, Frey AR, Coppens AB, Sanders J V. Fundamentals of acoustics. 4th editio. John Wiley & Sons; 2000.

# Appendix

An outline of the imaging process is given below. For the data presented in this paper, the average number of ray paths calculated to generate a single 3D TFM image for an individual array position over both imaging stages was approximately 41 billion. Due to this large amount of computationally-intensive calculations required and the independent nature of the TOF and TFM image calculations, the parallel computing platform CUDA was used to provide a huge processing speed up on the graphics processing unit (GPU).

(M) represents calculations in MATLAB on the central processing unit (CPU) and (C) represents calculations using CUDA on the GPU.

1. Initialise the scanning tank by mounting and orientating the array parallel to the back wall of the specimen using a B-scan image. Calculate velocities of sound in water and the specimen material.
2. Scan over the entire surface of the specimen in increments equal to half of the diameter of the active region of the array, collecting an FMC dataset at each array position.
3. (M) Load all FMC datasets, filter time-data and define imaging parameters.
4. (C) Calculate TOFs for the surface region at each array position and generate single-medium 3D TFM images using each FMC dataset and the velocity of sound in water. [section 3.1]

[The output for $N$ array positions is $N$ 3D surface TFM images.]

5. (M) Stitch $N$ surface TFM images into a stitched 3D TFM image of the entire surface.
6. (M) Extract surface points from stitched TFM image. [section 3.1]

[Output is $(x, y, z)$ coordinates of the extracted surface.]

7. (M) Define a subset of the point cloud of extracted surface points for each array position and define interior imaging parameters.
8. (C) Calculate TOFs through the surface points for each FMC dataset and generate immersion 3D TFM images for each array position while compensating for the velocities of sound in each medium. [section 3.2]

[The output for $N$ array positions is $N$ 3D interior TFM images.]

9. Stitch $N$ interior TFM images into a stitched 3D TFM image of the interior of the specimen.